Efficient and stable large-area perovskite solar cells with inorganic charge extraction layers

Wei Chen,[1, 2]* Yongzhen Wu,[1]* Youfeng Yue,[1] Jian Liu,[1] Wenjun Zhang,[2] Xudong Yang,[3] Han Chen,[3] Enbing Bi,[3] Islam Ashraful,[1] Michael Grätzel,[4]† Liyuan Han[1,3]†

[1]Photovoltaic Materials Unit, National Institute for Materials Science, Tsukuba, Ibaraki 305-0047, Japan. [2]Michael Grätzel Centre for Mesoscopic Solar Cells, Wuhan National Laboratory for Optoelectronics, Huazhong University of Science and Technology, Wuhan, China. [3]State Key Laboratory of Metal Matrix Composites, Shanghai Jiao Tong University, 800 Dong Chuan Road, Minhang District, Shanghai 200240, China. [4]Laboratory of Photonics and Interfaces, Department of Chemistry and Chemical Engineering, Swiss Federal Institute of Technology, Station 6, CH-1015 Lausanne, Switzerland.

*These authors contributed equally to this work.

†Corresponding author. E-mail: michael.graetzel@epfl.ch (M.G.); han.liyuan@nims.go.jp (L.H.)

The recent stunning rise in power conversion efficiencies (*PCE*s) of perovskite solar cells (PSCs) has triggered worldwide intense research. However, high *PCE* values have often been reached with poor stability at an illuminated area of typically less than 0.1 cm². We used heavily doped inorganic charge extraction layers in planar PSCs to achieve very rapid carrier extraction even with 10-20 nm thick layers avoiding pinholes and eliminating local structural defects over large areas. This robust inorganic nature allowed for the fabrication of PSCs with an aperture area >1 cm² showing a power conversion efficiency (*PCE*) >15% certified by an accredited photovoltaic calibration laboratory. Hysteresis in the current-voltage characteristics was eliminated; the PSCs were stable: >90% of the initial *PCE* remained after 1000 hours light soaking.

Organic–inorganic metal halide perovskite solar cells (PSCs) have attracted large attention due to the meteoric rise in their solar to electric power conversion efficiency (*PCE*) over the last few years (*1*). In particular, methylammoniun (CH₃NH₃PbI₃, denoted as MAPbI₃) and formamidinium lead iodide (CH(NH₂)₂PbI₃) emerged as a highly attractive solar light harvesting materials because of their intense broad–band absorption, high charge carrier mobility, low–cost precursor materials and simple solution processing (*2, 3*). Their ambipolar semiconducting characteristics further enable variable device architectures, ranging from mesoscopic to planar structures with n–i–p or p–i–n layouts (*4*). Mesoporous TiO₂-based PSCs have reached the highest performance (*5–7*); their certified *PCE* attaining presently 20.1% (*8*). However, there is growing interest in inverted (p–i–n) planar device architectures typically employing a MAPbI₃–PCBM ([6,6]–phenyl–C₆₁– butyric acid methyl ester) bilayer junction, because of their simple fabrication and relatively small hysteresis (*9–11*). A key question that remains open to date is the true power conversion efficiency and stability of planar PSCs as none of the devices has been certified so far and their stability remains largely unexplored. Only hole–conductor–free mesoscopic PSCs using carbon as a back contact have shown so far promising stability under long term light soaking and long term heat exposure, but their certified *PCE* remains relatively low at 12.8% (*12, 13*).

Regardless of their architectures, all high efficiency PSCs so far employed small areas, their device size being often <0.1 cm² (Table S1) (*14*). As such a small device size is prone to induce measurement errors, an obligatory minimum cell area of >1 cm² is required for certified *PCE*s to be recorded in the standard "Solar Cell Efficiency Tables" edited by public test centers, such as National Renewable Energy Laboratory (NREL) in the US and the National Institute of Advanced Industrial Science and Technology (AIST) in Japan (*15*). It has been recommended that the record efficiencies should be recorded with cell size of ideally 1 to 2 cm² or larger to allow comparison of competing technologies (*16–19*). Although a few works reported attempts of fabricating centimeter-scale PSCs, for example by using vacuum evaporation system (*20*) or modified two-step approach (*21*) to produce large area MAPbI₃ films, the *PCEs* obtained for these devices reached only 10.9%~12.6%. Apart from the small device areas, the widely recognized hysteresis and stability issues of PSCs have raised doubts on the reliability of previously claimed high efficiencies (*22, 23*).

The poor reproducibility and lack of uniformity of PSCs render it challenging to obtain high efficiencies with large devices. It is difficult to control the formation of cracks and pinholes in the selective carrier extraction layers over large areas. As small size PSCs typically show a wide spread in their *PCE*s, previous work has focused on improving the uniformity of perovskite layer by varying its deposition methods (*3, 6, 10*). However, fewer studies have aimed at identifying selective extraction layers for photogenerated charge carriers placed over the current collector to prevent their recombination at its surface (*24–26*); event though such selective contacts have turned out to be equally important to developing efficient solar light harvesters (*27*). The dilemma with optimizing of such charge carrier extraction layers in solar cells is that the film should be thin to

mimimize resistive losses while at the same time it should cover the whole collector area in a contiguous and uniform manner. Meeting these requirement becomes increasingly difficult as the device area increases.

Here we present a strategy that addresses simultaneously the scale up and stability issues facing current PSC embodiments. We develop heavily p–doped (p^+) $Ni_xMg_{1-x}O$ and n–doped (n^+) TiO_x contacts to extract selectively photogenerated charge carriers from an inverted planar $MAPbI_3$–PCBM film architecture. We implement the p^+ and n^+ doping by substituting $Ni(Mg)^{2+}$ ions and Ti^{4+} ions on the $Ni_xMg_{1-x}O$ lattice and TiO_x matrix by Li^+ and Nb^{5+} ions, respectively. The resulting dramatic increase in the electrical conductivity enables 10-20 nm thick oxide layers to be used for selective extraction of one type of charge carriers while improving their electronic blocking effect for the other type by reducing the density of pinholes and cracks over large areas. Accordingly, the series resistance (R_s) of the oxides decreased and the shunt resistance (R_{sh}) greatly increased with respect to the undoped ones, allowing excellent fill factor (FF) with values exceeding 0.8 and hysteresis–free behavior to be achieved. With this strategy, we successfully fabricated large size (>1 cm^2) PSCs with an efficiency of up to 16.2%. A *PCE* of 15% was certified by a public test center (Calibration, Standards and Measurement Team at the Research Center for Photovoltaics, National Institute of Advanced Industrial Science and Technology, AIST, Japan). This is listed as the first official efficiency entry for PSCs in the most recent edition of the "Solar Cell Efficiency Tables" (*28*). Moreover, the devices based on these stable p^+ and n^+ doped inorganic metal oxides charge extraction layers show high stability rendering them attractive for future practical deployment of PSCs.

We fabricated PSCs with an inverted planar device architecture (Fig. 1A); a cross sectional scanning electron microscopy (SEM) image of the device is shown in Fig. 1B. We first deposited the NiO based hole extraction layer onto fluorine-doped tin oxide (FTO) glass using spray pyrolysis. The precursor solution was composed of nickel (II) acetylacetonate alone or together with doping cations (Mg^{2+} from magnesium acetate tetrahydrate, Li^+ from lithium acetate) in super–dehydrated acetonitrile/ethanol mixture. The $MAPbI_3$ perovskite layer with thickness of ~300 nm was deposited by a reported method (*6*), which was followed by the deposition of a thin PCBM layer (80 nm) via spin–coating its chlorobenzol solution (20 mg ml^{-1}) at 1000 rpm for 30 s. An n–type TiO_x based electron extraction layer with and without Nb^{5+} doping was further deposited on the PCBM by spin–coating a diluted methanol solution of titanium isopropoxide (or mixed with niobium ethoxide), followed by controlled hydrolysis and condensation (*14*). Finally, the device was completed by thermal evaporation of a 100 nm thick Ag cathode. The band alignments of relevant functional layers are shown in Fig. 1C, based on the energy levels determined by ultraviolet (UV) photoelectron spectroscopy (UPS) and ul-

traviolet–visible (UV–Vis) absorption spectroscopy measurements (fig. S1) (*14*). The uniformity of the perovskite and PCBM layers was examined by cross sectional SEM observation (fig. S2) (*14*). The full XPS spectra of the NiO and TiO_x based charge carrier extraction layers are shown in fig. S3 (*14*), revealing the designated compositions for the target materials. The close–up observation on the morphology of the charge carrier extraction layers are depicted in fig. S4 (*14*), while their pin–hole densities were examined by electrical measurement as discussed below.

The stoichiometric form of NiO is a wide band gap semiconductor with a very low intrinsic conductivity of 10^{-13} S cm^{-1} (*29*). Self–doping by introducing Ni^{3+} acceptors into the NiO crystal lattice renders the crystals more conductive, depending on the film deposition techniques and conditions (*11*, *30–32*). The room temperature specific conductivity of our NiO films from Hall effect measurements was 1.66 × 10^{-4} S cm^{-1}. This value is much lower than the typically used p–type contact layer of PEDOT: PSS that shows a conductivity of 1 to 1000 S cm^{-1} (*33*). The low conductivity of NiO will lead to a high R_s resulting in a low *FF* of the solar cells (*34*). Substitutional doping by Li^+ is an effective way to increase the p-conductivity of NiO (*35*). Values of heavily (p^+)–doped NiO films can reach 1 to 10 S cm^{-1} at room temperature under optimal conditions (*36*). For our Li^+ doped $Ni_xMg_{1-x}O$ films the conductivity is 2.32 × 10^{-3} S cm^{-1}, ~12 times greater than that of the undoped reference.

A Mg^{2+} content of 15 mol% was alloyed in the Li^+ doped nickel oxide film, to compensate the undesirable positive shift of its valence band (E_{VB}) caused by Li^+ incorporation into the lattice (fig. S1) (*14*, *35*, *37*, *38*). As the Li^+ content was adjusted to 5 mol%, the doped oxide has the formula of $Li_{0.05}Mg_{0.15}Ni_{0.8}O$ if one assumes that the molar ratio of the three different cations in the spray pyrolyses solution is maintained in the mixed oxide. This co–doping strategy is feasible because the mismatch of the ionic radii of Li^+ (0.76Å), Mg^{2+} (0.71Å) and Ni^{2+} (0.69Å) is quite small, conferring good lattice stability to the $Li_xMg_yNi_{1-x-y}O$ ternary oxides. We compared conductivity of NiO and $Li_{0.05}Mg_{0.15}Ni_{0.8}O$ films by using contact–current mode of a scanning probe microscope (SPM) and show the results in Fig. 2, A and B. At a bias potential of 1.0 V, the electric current increased by a factor of ~10 (from ~0.3 nA to ~3 nA) upon replacing undoped NiO by a $Li_{0.05}Mg_{0.15}Ni_{0.8}O$ film. The XPS spectra in fig. S6 (*14*) reveal that the doping increased the relative content of Ni^{3+} acceptors in the $Li_{0.05}Mg_{0.15}Ni_{0.8}O$ sample. These findings are consistent with reports on Li^+ doped NiO films in (*32*) and explains the increase in carrier concentration from 2.66 × 10^{17} cm^{-3} of the undoped NiO film to 6.46 × 10^{18} cm^{-3} for $Li_{0.05}Mg_{0.15}Ni_{0.8}O$ film that we derived from Hall effect measurements.

The electron specific n–type TiO_x contact used commonly for organic PV is normally fabricated by hydrolysis and condensation of titanium alkoxides at temperature below 150°C (*39*, *40*), where the crystallization of TiO_2 is slow. In order to

prevent heat-induced degradation of the perovskite layer and the adjacent interfaces, we kept the annealing temperature of TiO_x films below 70°C. While such TiO_x films have been used extensively in organic PVs, details on their structure and mechanism of electric conduction have so far not been elucidated (*41*). One commonly recognized problem is that the amorphous nature of TiO_x leads to extremely low specific conductivities that are in the range of 10^{-8}–10^{-6} S cm^{-1} (*42*). Nb^{5+} doping has proved to be effective for enhancing the conductivity of crystalline anatase TiO_2 films to $\sim 10^4$ S cm^{-1}, enabling its use as a transparent conducting oxide similar to conventional indium tin oxide (*43*). By analogy, this dopant is expected to improve also the conductivity of the amorphous TiO_x via substitution of Ti^{4+} by Nb^{5+} which is expected to create donor centers. From the current-voltage (*I–V*) curves obtained by SPM measurement shown in Fig. 2B, the conductivity of TiO_x film was estimated to increase from about 10^{-6} S cm^{-1} to 10^{-5} S cm^{-1} upon adding 5 mol% Nb^{5+} to the precursor solution. By resolving the XPS spectra in fig. S6 (*14*), the relative content of Ti^{3+} in comparison to Ti^{4+}, i.e., the donor species in the TiO_x film responsible for its n–type conductivity, has increased via Nb^{5+} doping.

We derived the optimal thickness of the NiO- and TiO_x-based charge-extraction layers from the electrical measurements shown in fig. S7 (*14*). A complete layer with no pinholes of NiO and TiO_x requires at least thickness of 20 nm and 10 nm, respectively, regardless of the presence of dopants. These minimum thicknesses should depend on the underlayers' (FTO for NiO, or PCBM for TiO_x) surface chemistry and morphology, as well as the fabrication methods used for the NiO and TiO_x films. We compared small solar cells with size of 0.09 cm^2 and varied the NiO layer thickness from 10, 20 to 40 nm, keeping that of the $Ti_{0.95}Nb_{0.05}O_x$ fixed at 10 nm. Conversely, we fixed the $Li_{0.05}Mg_{0.15}Ni_{0.8}O$ layer thickness at 20 nm and varied that of the TiO_x films from 5 to 30 nm. For each condition, 20 cells were made and measured to establish any underlying trends. As shown in fig. S8 (*14*), although high performance can be occasionally achieved from devices with very thin charge carrier extraction layers (~10 nm NiO or ~5 nm TiO_x), most devices showed lower *PCE*s because of lower *FF* and open–circuit voltage (*V*$_{oc}$) (fig. S9) (*14*), which can be attributed to the presence of substantial levels of pinholes. The reproducibility of device performance was greatly enhanced as the thickness of charge extraction layers increased, while the optimal performance was attained with 20 nm NiO and 10 nm TiO_x film, in agreement with the electrical measurement. Further increasing the film thickness of the two charge extraction layers can lead to a large efficiency decline caused by increased internal resistance, larger optical loss, or both (fig. S10) (*14*). Thus, we fixed the thickness of NiO and TiO_x at 20 nm and 10 nm, respectively for the following studies of doping effect on device performance.

Figure 3A shows the effect of doping the NiO and TiO_x charge extraction layers on the photocurrent density–voltage (*J–V*) curves of PSCs measured under simulated AM 1.5 sunlight with forward scanning direction. The short circuit current (*J*$_{sc}$), *V*$_{oc}$, *FF*, and *PCE* data are listed in Table S2 (*14*). Both doping of NiO and TiO_x reduced R_s and improved the *FF*, and to a lesser extent *J*$_{sc}$ and *V*$_{oc}$. The TiO_x electron extraction layers mainly affect the shape of *J–V* curves in the forward bias range from 0.7 to 1.0 V, where a Schottky-barrier type contact between PCBM and Ag strongly restricted efficient electron collection (fig. S9A) (*14*, *44*). The Nb^{5+} doping of TiO_x reduced the interfacial electron transfer resistance and facilitated electron transport, increasing the photocurrent especially in the 0.7 to 1.0 V forward bias region. The NiMg(Li)O-based hole extraction layer promoted ohmic contact formation at the FTO–$MAPbI_3$ interface by decreasing the barrier height through the staircase energy level alignment shown in Fig. 1C. P^+–doping increased the electrical conductivity by decreasing the charge transport resistance and hence enhancing hole extraction.

Doping of both NiO and TiO_x improves the cell performance by increasing the values of *FF* and *V*$_{oc}$ to 0.827 and 1.083 V, respectively, leading to *PCE* of 18.3% for this planar PSC with $MAPbI_3$. In comparison to PEDOT:PSS based PSCs, the *V*$_{oc}$ increased by ~100 mV, indicating that with $Li_{0.05}Mg_{0.15}Ni_{0.8}O$, the holes can be extracted at a higher energy level (*10*). Furthermore, the *FF* of 0.83 is one of the highest values for reported PSCs (*8*, *9*, *23*), demonstrating the key role of the charge extraction layers in minimizing resistive losses and improving the photovoltaic performance.

To gain further insight into the reasons for the performance enhancement by the doping, we characterized the charge carrier extraction, transportation and recombination by nanosecond time–resolved photoluminescence (PL) decay using a picosecond laser flash as excitation source and by measuring transient photocurrent/photovoltage decays on the microsecond scale. The charge extraction involved in our cells include the electron transfer from the $MAPbI_3$ absorber layer to PCBM/TiO_x and hole transfer to NiO as well as the carrier transport in the TiOx and NiMg(Li)O layers. The perovskite/PCBM interface has been demonstrated to be very efficient for electron extraction (*9–11*). Doping of the TiO_x extraction layer is unlikely to have a direct impact on the electron injection rate because of it physical separation from the $MAPbI_3$ by 80 nm-thick PCBM layer. Nevertheless, it greatly accelerates the electron extraction by decreasing the electron transport time as shown in Fig. 3C. Figure 3B shows the PL decays of the $MAPbI_3$ films on different substrates, including a glass slide, and NiO and $Li_{0.05}Mg_{0.15}Ni_{0.8}O$ deposited on FTO glass. The $MAPbI_3$ itself showed a long PL lifetime of >100 ns, indicating slow carrier recombination in the perovskite layer (*10*). When contacted with the p–type hole extraction layers, the PL lifetimes were shortened to a similar degree for both doped and undoped NiO–$MAPbI_3$ contacts. Thus, doping has a negligible influence on the hole injection.

We derived the charge transport and recombination time constants (τ_t and τ_r) from the transient photocurrent and photovoltage decays measured at short and open circuit, respectively (Fig. 3C). The τ_t decreased by ~5 fold from 4.41 μs for undoped cell to 0.88 μs for doped cell, confirming the much faster charge transport through the doped charge carrier extraction layers compared to the undoped ones. However, the τ_r of a doped cell is substantially longer than that of an undoped one (84.8 vs. 50.5 μs, Fig. 3D), which we attribute to slower interfacial charge recombination since the very rapid carrier collection prevents charge accumulation at the interface of the pervovskite with the charge extraction layer. The doping-induced difference in charge transport/recombination kinetics should be the main reason responsible for their performance enhancement.

The hysteresis of our cells was examined by using different scan rates and directions. By decreasing the step width from 70 mV to 5 mV, the *PCE*s determined from the forward scan slightly increased from 18.14% to 18.35%. However, the reverse scan *PCE*s decreased substantially from 22.35% at 70 mV/step (fig. S11A and table S3 (*14*)) to 18.40% at 5 mV/step. The steady power outputs measurements (fig. S11D) (*14*) indicate that the *PCE*s obtained in forward scans and at small step widths (5–10 mV) are near the real performance. The V_{oc} and *PCE* obtained at a fast reverse scan, *i.e.*, 1.273 V and 22.35% at 70 mV/step, are largely overestimated. With the step widths of 5–10 mV, the *PCE* deviations between forward and reverse scans are very small, *i.e.*, within 0.3% in absolute *PCE* values reflecting negligible hysteresis. A histogram comparing the difference in the *PCE*s obtained from scanning in the forward and reverse bias directions is shown in fig. S11C (*14*), supporting the absence of hysteresis for the optimized device architecture. In stark contrast, for undoped charge extraction layers, a pronounced hysteresis was observed even for slow scan rates (fig. S11E) (*14*), which is likely to arise from unbalanced charge accumulation at the two interfaces (*45*). Thus, the $Li_{0.05}Mg_{0.15}Ni_{0.8}O$ and $Ti_{0.95}Nb_{0.05}O_x$ charge extraction layer create a robust low impedance interface that can mitigate the *J–V* hysteresis under a routine scanning condition.

We fabricate cells with active area >1 cm² as a first step toward scale up of the photovoltaic devices. Figure 4A shows the *J–V* curve of such cell with aperture area of 1.02 cm². It shows excellent performance, with J_{sc}, V_{oc}, and *FF* reaching values of 20.21 mA cm⁻², 1.072 V and 0.748, respectively, corresponding to a *PCE* of 16.2%. Hysteresis for these large area devices is also small (fig. S12) (*14*). The corresponding *IPCE* (Fig. 4B) shows a broad plateau with maximum value of 90.1% over practically the whole visible range. The integrated J_{sc} from *IPCE* matches well with the measured value. Compared to small size cells (0.09 cm²), a ~10% decrease in *PCE* was observed in large size cells (1.02 cm²), which is mainly caused by the large sheet resistance of the FTO. We sent one of our best large cells to a public test center (AIST, Japan) for certification. A *PCE* of 15.0% for a 1.017 cm² device was certified (fig. S13) (*14*).

To demonstrate the superiority of the solution processible $Ti_{0.95}Nb_{0.05}O_x$ charge carrier extraction layer, two references, *i.e.*, Ca (4nm)/Ag, LiF (1.5nm)/Ag that were deposited by thermal evaporation, were compared with our best interfacial condition. As shown in Fig. 4C, without sealing, the Ti(Nb)Oₓ based PSC shows the best stability since its *PCE* only decreased by ~5% of its initial value after 1 week. The Ca/Ag based PSC showed the fastest degradation, which lost its initial *PCE* by >30% after 1 day and by ~45% within 1 week. This difference is attributed to the fast oxidization of very reactive Ca, leading to dramatic loss on J_{sc} and *FF*. The LiF/Ag based PSC lost 15% of its initial *PCE* within 1 week. The extremely thin LiF layer (< 2.5 nm, as required by efficient tunneling) (*46*) and the high sensitivity of LiF to moisture is likely to be responsible for the corresponding cell's inferior stability. It is possible that the stability of Ca or LiF based devices can be improved if they are thoroughly sealed. However, the requirement on sealing quality will be much more critical in comparison to the air–stable interface of $Ti_{0.95}Nb_{0.05}O_x$ (*39*).

The $Ti_{0.95}Nb_{0.05}O_x$ layer also shields the perovskite from the intrusion of humidity. It assumes a similar role in OPVs (*39*). We exposed bare $MAPbI_3$, $MAPbI_3$/PCBM and $MAPbI_3$/PCBM/Ti(Nb)Oₓ, to ambient air under room light for 3 weeks. A striking difference in color degradation associated with perovskite decomposition became clearly visible (fig. S14) (*14*). Thus it appears that the hydrophobic nature of PCBM may protect the perovskite from reaction with water, while the coating of Ti(Nb)Oₓ could further enhance the stability.

Figure 4D also shows the long–term stability of PSCs using the optimized inorganic charge extraction layers. The silver back contact was protected by a covering glass which was separated from the front FTO glass by a UV-activated glue used as a sealant. The cells maintained 97% of their initial *PCE* after keeping them in the dark for 1000 hours. Exposing the cells for 1000 hours at short–circuit condition to full sunlight from a solar simulator, resulted in a *PCE* degradation of less than 10%. This degradation is consistent with the general tendency among 10 devices, as shown in fig. S15 (*14*), indicative of their good long-term stability. During this time, an electric charge of around 72'000 C (4.49 × 10²³ electrons) passed through the device. This result shows that the planar cell structure and the metal oxides extraction layers, as well as the organo–metal halide perovskite material, are robust enough to sustain continued current flow under light exposure for 1000 hours. A further increase in the *PCE* without sacrificing stability could be expected from varying the composition of the pervoskite, e.g., replacing part of the methylammonium cations in the $MAPbI_3$ pervovskite by formamidinium (*47*) and a small fraction of the iodide by bromide anions.

REFERENCES AND NOTES

1. G. Hodes, Perovskite-based solar cells. *Science* **342**, 317–318 (2013). Medline

doi:10.1126/science.1245473

2. G. Xing, N. Mathews, S. Sun, S. S. Lim, Y. M. Lam, M. Grätzel, S. Mhaisalkar, T. C. Sum, Long-range balanced electron- and hole-transport lengths in organic-inorganic $CH_3NH_3PbI_3$. *Science* **342**, 344–347 (2013). Medline

3. Q. Dong, Y. Fang, Y. Shao, P. Mulligan, J. Qiu, L. Cao, J. Huang, Electron-hole diffusion lengths > 175 μm in solution-grown $CH_3NH_3PbI_3$ single crystals. *Science* **347**, 967–970 (2015). Medline doi:10.1126/science.aaa5760

4. M. Liu, M. B. Johnston, H. J. Snaith, Efficient planar heterojunction perovskite solar cells by vapour deposition. *Nature* **501**, 395–398 (2013). Medline doi:10.1038/nature12509

5. J. Burschka, N. Pellet, S. J. Moon, R. Humphry-Baker, P. Gao, M. K. Nazeeruddin, M. Grätzel, Sequential deposition as a route to high-performance perovskite-sensitized solar cells. *Nature* **499**, 316–319 (2013). Medline doi:10.1038/nature12340

6. N. J. Jeon, J. H. Noh, Y. C. Kim, W. S. Yang, S. Ryu, S. I. Seok, Solvent engineering for high-performance inorganic-organic hybrid perovskite solar cells. *Nat. Mater.* **13**, 897–903 (2014). Medline doi:10.1038/nmat4014

7. N. J. Jeon, J. H. Noh, W. S. Yang, Y. C. Kim, S. Ryu, J. Seo, S. I. Seok, Compositional engineering of perovskite materials for high-performance solar cells. *Nature* **517**, 476–480 (2015). Medline doi:10.1038/nature14133

8. W. S. Yang, J. H. Noh, N. J. Jeon, Y. C. Kim, S. Ryu, J. Seo, S. I. Seok, High-performance photovoltaic perovskite layers fabricated through intramolecular exchange. *Science* **348**, 1234–1237 (2015). Medline doi:10.1126/science.aaa9272

9. J. H. Heo, H. J. Han, D. Kim, T. K. Ahn, S. H. Im, Stable semi-transparent $CH_3NH_3PbI_3$ planar sandwich solar cells. *Energy Environ. Sci.* **8**, 1602–1608 (2015).

10. W. Nie, H. Tsai, R. Asadpour, J. C. Blancon, A. J. Neukirch, G. Gupta, J. J. Crochet, M. Chhowalla, S. Tretiak, M. A. Alam, H. L. Wang, A. D. Mohite, High-efficiency solution-processed perovskite solar cells with millimeter-scale grains. *Science* **347**, 522–525 (2015). Medline doi:10.1126/science.aaa0472

11. J. H. Park, J. Seo, S. Park, S. S. Shin, Y. C. Kim, N. J. Jeon, H. W. Shin, T. K. Ahn, J. H. Noh, S. C. Yoon, C. S. Hwang, S. I. Seok, Efficient $CH_3NH_3PbI_3$ perovskite solar cells employing nanostructured p-type NiO electrode formed by a pulsed laser deposition. *Adv. Mater.* **27**, 4013–4019 (2015). Medline doi:10.1002/adma.201500523

12. A. Mei, X. Li, L. Liu, Z. Ku, T. Liu, Y. Rong, M. Xu, M. Hu, J. Chen, Y. Yang, M. Grätzel, H. Han, A hole-conductor–free, fully printable mesoscopic perovskite solar cell with high stability. *Science* **345**, 295–298 (2014). Medline

13. X. Li, M. Tschumi, H. Han, S. S. Babkair, R. A. Alzubaydi, A. A. Ansari, S. S. Habib, M. K. Nazeeruddin, S. M. Zakeeruddin, M. Grätzel, Outdoor performance and stability under elevated temperatures and long-term light soaking of triple-layer mesoporous perovskite photovoltaics. *Energy Technol.* **3**, 551–555 (2015). doi:10.1002/ente.201500045

14. Materials and methods are available as supplementary materials on *Science* Online.

15. M. A. Green, K. Emery, Y. Hishikawa, W. Warta, E. D. Dunlop, Solar cell efficiency tables (Version 45). *Prog. Photovolt. Res. Appl.* **23**, 1–9 (2015). doi:10.1002/pip.2573

16. M. C. Beard, J. M. Luther, A. J. Nozik, The promise and challenge of nanostructured solar cells. *Nat. Nanotechnol.* **9**, 951–954 (2014). Medline doi:10.1038/nnano.2014.292

17. E. Zimmermann, P. Ehrenreich, T. Pfadler, J. A. Dorman, J. Weickert, L. Schmidt-Mende, Erroneous efficiency reports harm organic solar cell research. *Nat. Photonics* **8**, 669–672 (2014). doi:10.1038/nphoton.2014.210

18. K. D. G. I. Jayawardena, L. J. Rozanski, C. A. Mills, S. R. P. Silva, The true status of solar cell technology. *Nat. Photonics* **9**, 207–208 (2015). doi:10.1038/nphoton.2015.45

19. Bringing solar cell efficiencies into the light. *Nat. Nanotechnol.* **9**, 657 (2014).

20. O. Malinkiewicz, C. Roldán-Carmona, A. Soriano, E. Bandiello, L. Camacho, M. K. Nazeeruddin, H. J. Bolink, Metal-oxide-free methylammonium lead iodide perovskite-based solar cells: The influence of organic charge transport layers. *Adv. Energy Mater.* **4**, 1400345 (2014). doi:10.1002/aenm.201400345

21. Z. Yang, B. Cai, B. Zhou, T. Yao, W. Yu, S. F. Liu, W.-H. Zhang, C. Li, An up-scalable approach to $CH_3NH_3PbI_3$ compact films for high-performance perovskite solar cells. *Nano Energy* **15**, 670–678 (2015). doi:10.1016/j.nanoen.2015.05.027

22. M. Grätzel, The light and shade of perovskite solar cells. *Nat. Mater.* **13**, 838–842 (2014). Medline doi:10.1038/nmat4065

23. M. Gunther, "Meteoritic rise of perovskite solar cells under scrutiny over efficiencies," *Chemistry World*, 2 March 2015; www.rsc.org/chemistryworld/2015/02/meteoritic-rise-perovskite-solar-cells-under-scrutiny-over-efficiencies.

24. H. Zhou, Q. Chen, G. Li, S. Luo, T. B. Song, H. S. Duan, Z. Hong, J. You, Y. Liu, Y. Yang, Interface engineering of highly efficient perovskite solar cells. *Science* **345**, 542–546 (2014). Medline doi:10.1126/science.1254050

25. O. Malinkiewicz, A. Yella, Y. H. Lee, G. M. Espallargas, M. Graetzel, M. K. Nazeeruddin, H. J. Bolink, Perovskite solar cells employing organic charge-transport layers. *Nat. Photonics* **8**, 128–132 (2014). doi:10.1038/nphoton.2013.341

26. Q. Lin, A. Armin, R. C. R. Nagiri, P. L. Burn, P. Meredith, Electro-optics of perovskite solar cells. *Nat. Photonics* **9**, 106–112 (2015). doi:10.1038/nphoton.2014.284

27. A. G. Aberle, Surface passivation of crystalline silicon solar cells: A review. *Prog. Photovolt. Res. Appl.* **8**, 473–487 (2000). doi:10.1002/1099-159X(200009/10)8:5<473::AID-PIP337>3.0.CO;2-D

28. M. A. Green, K. Emery, Y. Hishikawa, W. Warta, E. D. Dunlop, Solar cell efficiency tables (version 46). *Prog. Photovolt. Res. Appl.* **23**, 805–812 (2015). doi:10.1002/pip.2637

29. M. A. Wittenauer, L. L. Van Zandt, Surface conduction versus bulk conduction in pure stoichiometric NiO crystals. *Philos. Mag. B* **46**, 659–667 (1982). doi:10.1080/01418638208223551

30. J. H. Kim, P. W. Liang, S. T. Williams, N. Cho, C. C. Chueh, M. S. Glaz, D. S. Ginger, A. K. Jen, High-performance and environmentally stable planar heterojunction perovskite solar cells based on a solution-processed copper-doped nickel oxide hole-transporting layer. *Adv. Mater.* **27**, 695–701 (2015). Medline doi:10.1002/adma.201404189

31. Z. Zhu, Y. Bai, T. Zhang, Z. Liu, X. Long, Z. Wei, Z. Wang, L. Zhang, J. Wang, F. Yan, S. Yang, High-performance hole-extraction layer of sol–gel-processed NiO_x nanocrystals for inverted planar perovskite solar cells. *Angew. Chem. Int. Ed.* **53**, 12571–12575 (2014).

32. C. Wu, C. Yang, Effect of annealing temperature on the characteristics of the modified spray deposited Li-doped NiO films and their applications in transparent heterojunction diode. *Sol. Energy Mater. Sol. Cells* **132**, 492–498 (2015). doi:10.1016/j.solmat.2014.09.017

33. Y. H. Kim, C. Sachse, M. L. Machala, C. May, L. Müller-Meskamp, K. Leo, Highly conductive PEDOT:PSS electrode with optimized solvent and thermal post-treatment for ITO-free organic solar cells. *Adv. Funct. Mater.* **21**, 1076–1081 (2011). doi:10.1002/adfm.201002290

34. X. F. Chen, H. M. Huang, X. L. Li, G. J. Liu, H. Zhang, Slightly focused high-energy shockwave therapy: A potential adjuvant treatment for osteoporotic fracture. *Int. J. Clin. Exp. Med.* **8**, 5044–5054 (2015). Medline

35. N. Alidoust, M. C. Toroker, J. A. Keith, E. A. Carter, Significant reduction in NiO band gap upon formation of $Li_xNi_{1-x}O$ alloys: Applications to solar energy conversion. *ChemSusChem* **7**, 195–201 (2014). Medline doi:10.1002/cssc.201300595

36. U. S. Joshi, Y. Matsumoto, K. Itaka, M. Sumiya, H. Koinuma, Combinatorial synthesis of Li-doped NiO thin films and their transparent conducting properties. *Appl. Surf. Sci.* **252**, 2524–2528 (2006). doi:10.1016/j.apsusc.2005.03.239

37. Z. Huang, X. Zeng, X. Wang, W. Zhang, Y. Li, M. Wang, Y.-B. Cheng, W. Chen, Enhanced performance of p-type dye sensitized solar cells based on mesoporous $Ni_{1-x}Mg_xO$ ternary oxide films. *RSC Adv.* **4**, 60670–60674 (2014). doi:10.1039/C4RA09727K

38. J. Deng, M. Mortazavi, N. V. Medhekar, J. Zhe Liu, Band engineering of $Ni_{1-x}Mg_xO$ alloys for photocathodes of high efficiency dye-sensitized solar cells. *J. Appl. Phys.* **112**, 123703 (2012). doi:10.1063/1.4769210

39. K. Lee, J. Y. Kim, S. H. Park, S. H. Kim, S. Cho, A. J. Heeger, Air-stable polymer electronic devices. *Adv. Mater.* **19**, 2445–2449 (2007). doi:10.1002/adma.200602653

40. T. Kuwabara, T. Nakayama, K. Uozumi, T. Yamaguchi, K. Takahashi, Highly durable inverted-type organic solar cell using amorphous titanium oxide as electron collection electrode inserted between ITO and organic layer. *Sol. Energy Mater. Sol. Cells* **92**, 1476–1482 (2008). doi:10.1016/j.solmat.2008.06.012

41. T. Kuwabara, H. Sugiyama, T. Yamaguchi, K. Takahashi, Inverted type bulk-heterojunction organic solar cell using electrodeposited titanium oxide thin films as electron collector electrode. *Thin Solid Films* **517**, 3766–3769 (2009). doi:10.1016/j.tsf.2008.12.039

42. K. Wojciechowski, M. Saliba, T. Leijtens, A. Abate, H. J. Snaith, Sub-150 °C processed meso-superstructured perovskite solar cells with enhanced efficiency. *Energy Environ. Sci.* **7**, 1142–1147 (2014).

43. Y. Furubayashi, T. Hitosugi, Y. Yamamoto, K. Inaba, G. Kinoda, Y. Hirose, T. Shimada, T. Hasegawa, A transparent metal: Nb-doped anatase TiO$_2$. *Appl. Phys. Lett.* **86**, 252101–252103 (2005). doi:10.1063/1.1949728

44. S. Braun, W. R. Salaneck, M. Fahlman, Energy-level alignment at organic/metal and organic/organic interfaces. *Adv. Mater.* **21**, 1450–1472 (2009). doi:10.1002/adma.200802893

45. J. H. Heo, D. H. Song, H. J. Han, S. Y. Kim, J. H. Kim, D. Kim, H. W. Shin, T. K. Ahn, C. Wolf, T. W. Lee, S. H. Im, Planar CH$_3$NH$_3$PbI$_3$ perovskite solar cells with constant 17.2% average power conversion efficiency irrespective of the scan rate. *Adv. Mater.* **27**, 3424–3430 (2015). Medline doi:10.1002/adma.201500048

46. X. Liu, H. Yu, L. Yan, Q. Dong, Q. Wan, Y. Zhou, B. Song, Y. Li, Triple cathode buffer layers composed of PCBM, C$_{60}$, and LiF for high-performance planar perovskite solar cells. *ACS Appl. Mater. Interfaces* **7**, 6230–6237 (2015). Medline doi:10.1021/acsami.5b00468

47. J. Liu, Y. Shirai, X. Yang, Y. Yue, W. Chen, Y. Wu, A. Islam, L. Han, High-quality mixed-organic-cation perovskites from a phase-pure non-stoichiometric intermediate (FAI)$_{1−x}$-PbI$_2$ for solar cells. *Adv. Mater.* **27**, 4918–4923 (2015). Medline doi:10.1002/adma.201501489

48. P. Puspharajah, S. Radhakrishna, A. K. Arof, Transparent conducting lithium-doped nickel oxide thin films by spray pyrolysis technique. *J. Mater. Sci.* **32**, 3001–3006 (1997). doi:10.1023/A:1018657424566

49. T. Dutta, P. Gupta, A. Gupta, J. Narayan, Effect of Li doping in NiO thin films on its transparent and conducting properties and its application in heteroepitaxial p-n junctions. *J. Appl. Phys.* **108**, 083715 (2010). doi:10.1063/1.3499276

50. T. Moehl, J. H. Im, Y. H. Lee, K. Domanski, F. Giordano, S. M. Zakeeruddin, M. I. Dar, L. P. Heiniger, M. K. Nazeeruddin, N. G. Park, M. Grätzel, Strong photocurrent amplification in perovskite solar cells with a porous TiO2 blocking layer under reverse bias. *J. Phys. Chem. Lett.* **5**, 3931–3936 (2014). Medline

ACKNOWLEDGMENTS

SUPPLEMENTARY MATERIALS

www.sciencemag.org/cgi/content/full/science.aad1015/DC1
Materials and Methods
Figs. S1 to S15
Tables S1 to S3
References (*48–50*)

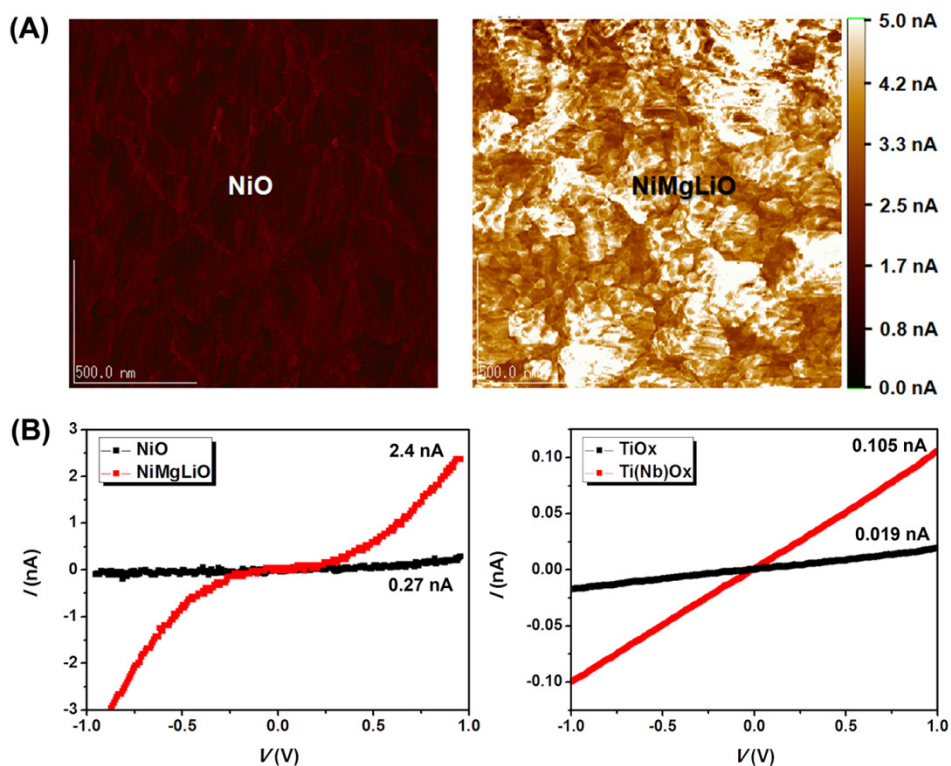Fig. 1. Structure and band alignments of the PSC. (A) Scheme of the cell configuration highlighting the doped charge carrier extraction layers. The right insets shows the composition of Ti(Nb)O$_x$ and the crystal structure of lithium doped Ni$_x$Mg$_{1-x}$O, denoted as NiMg(Li)O. (B) A high resolution cross–sectional SEM image of a complete solar cell (the corresponding EDX analysis results are shown in fig. S5 (14), demonstrating the presence of the p$^+$–doped Ni$_x$Mg$_{1-x}$O and n$^+$–doped TiO$_x$ charge extraction layers). (C) Band alignments of the solar cell. The data of MAPbI$_3$ and PCBM are taken from (11).

Fig. 2. Dopant enhanced conductivity of NiO and TiO$_x$. (A) Comparison of the conductivity mapping results for NiO (Left) and Li$_{0.05}$Mg$_{0.15}$Ni$_{0.8}$O (Right) films. (B) Left: Comparison of the $I-V$ curves of NiO and Li$_{0.05}$Mg$_{0.15}$Ni$_{0.8}$O films deposited on FTO glass and Right: Comparison of the $I-V$ curves for TiO$_x$ and Ti$_{0.95}$Nb$_{0.05}$O$_x$ films deposited on PCBM/ITO glass, obtained by SPM measurements. Thickness was 20 nm for both NiO and TiO$_x$ based films.
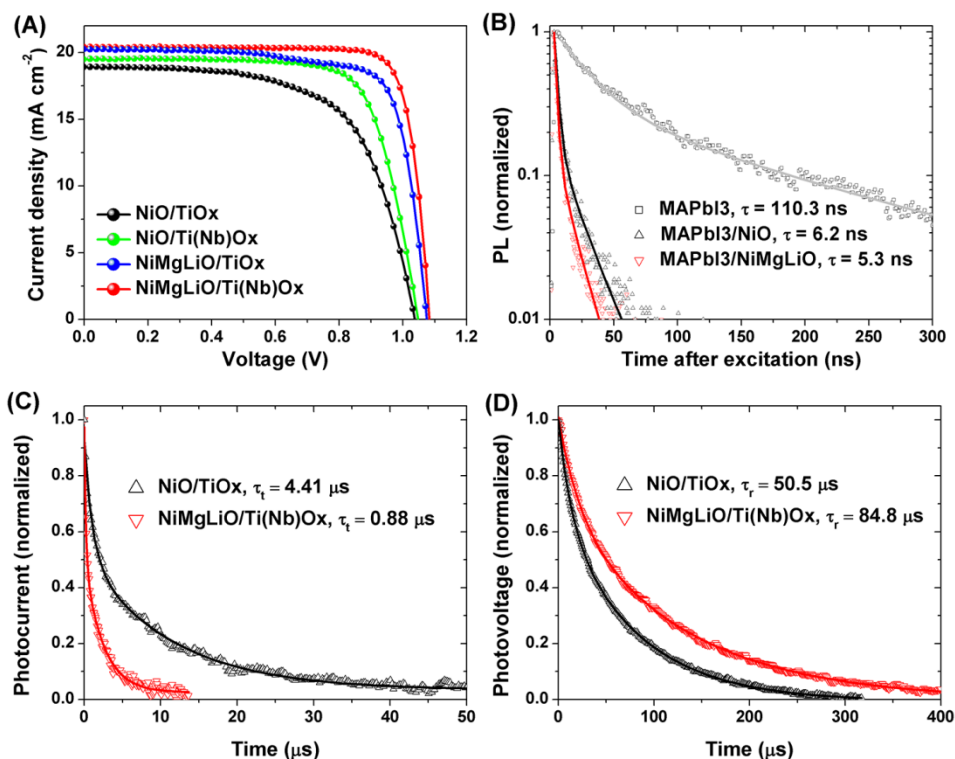
Fig. 3. Doping enhanced photovoltaic performance. (A) *J-V* curves of solar cells based on different combinations of charge extraction layers with standard thickness (NiO, NiMg(Li)O = 20 nm; TiO_x, $Ti(Nb)O_x$ = 10 nm). (B) Normalized PL transient decay curves of perovskite and perovskite at the controlled interfaces of NiO and NiMg(Li)O, solid lines are fitted results with a double exponential decay. The time interval during which the PL decays to 1/e of the initial intensity is defined as the characteristic lifetime (τ) of free carriers after photoexcitation. (C) and (D) show normalized transient photocurrent and photovoltage decay curves, respectibely based on undoped and doped charge carrier extraction layers. The charge transport (τ_t) and recombination time (τ_r) are again defined as the time interval during which the photocurrent or photovoltage decays to 1/e of the their initial value immediately after excitation.
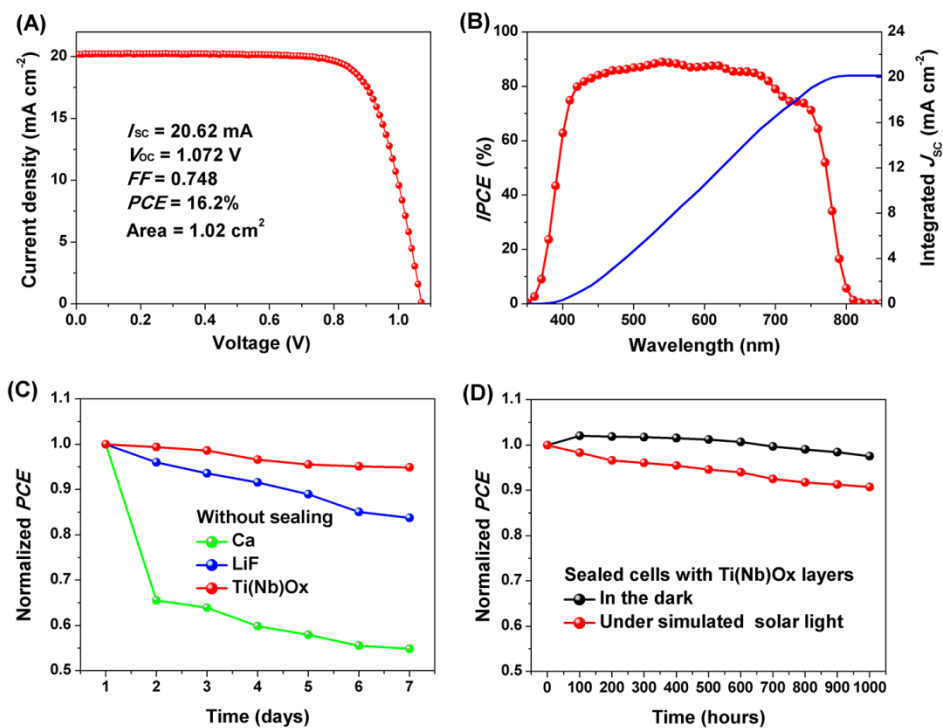
Fig. 4. Performance and stability of large size cells. (**A**) $J-V$ curve of the best large cell endowed with anti−reflection film, (**B**) the corresponding *IPCE* spectrum and integrated J_{sc}, (**C**) the stability of the cells without sealing, based on different electron extraction layers of Ca (4 nm), LiF (1.5 nm) and Ti(Nb)O$_x$ (10 nm) between PCBM and the Ag contact, the cells were kept in a dry cabinet (< 20% humidity) in the dark and measured in ambient air, (**D**) stability of sealed cells kept in the dark or under simulated solar light (AM 1.5, 100 mW cm^{-2}, using a 420 nm UV light cut−off filter, surface temperature of the cell: 45° to 50°C, bias potential = 0 V).